Ultramicroscopy 146 (2014) 117–124

Contents lists available at ScienceDirect

Ultramicroscopy

journal homepage: www.elsevier.com/locate/ultramic

Multi-actuation and PI control: A simple recipe for high-speed and large-range atomic force microscopy

I. Soltani Bozchalooi *, K. Youcef-Toumi

Department of Mechanical Engineering, Massachusetts Institute of Technology, Cambridge, MA 02139, USA

ARTICLE INFO

Article history:
Received 9 March 2014
Received in revised form
12 May 2014
Accepted 24 July 2014
Available online 11 August 2014

Keywords:
Multi-actuation
Dual actuation
Resonance compensation
Dynamics compensation
High-speed AFM imaging
Data-based control design

ABSTRACT

High speed atomic force microscopy enables observation of dynamic nano-scale processes. However, maintaining a minimal interaction force between the sample and the probe is challenging at high speed specially when using conventional piezo-tubes. While rigid AFM scanners are operational at high speeds with the drawback of reduced tracking range, multi-actuation schemes have shown potential for high-speed and large-range imaging. Here we present a method to seamlessly incorporate additional actuators into conventional AFMs. The equivalent behavior of the resulting multi-actuated setup resembles that of a single high-speed and large-range actuator with maximally flat frequency response. To achieve this, the dynamics of the individual actuators and their couplings are treated through a simple control scheme. Upon the implementation of the proposed technique, commonly used PI controllers are able to meet the requirements of high-speed imaging. This forms an ideal platform for retroactive enhancement of existing AFMs with minimal cost and without compromise on the tracking range. A conventional AFM with tube scanner is retroactively enhanced through the proposed method and shows an order of magnitude improvement in closed loop bandwidth performance while maintaining large range. The effectiveness of the method is demonstrated on various types of samples imaged in contact and tapping modes, in air and in liquid.

1. Introduction

Atomic force microscopy has helped us acquire better understanding of the nano-scale world [1]. High speed atomic force microcopy can extend the applications of this powerful instrument to the study of dynamic nano-scale processes [2]. However, the mechanical nature of AFM always introduces concern about the extent of probe-sample interaction and its influence on the reliability of acquired data. This is especially true at high imaging speeds and for more delicate samples such as biological samples [3,4]. In these applications the fast tracking of nano-scale features of the sample is expected to take place over a few microns of height variations on the sample due to sample thickness [5], or caused by sample tilt. This calls for simultaneous high-speed and large-range tracking capability of the AFM.

The effective approaches towards high-speed topography tracking have been mainly based on a bottom-up re-design of the AFM scanner [6–8]. The resulting AFM scanners, referred to as flexure-based or rigid, use small and short-range piezo actuators. The excitation of the structural dynamics in these scanner designs necessitate the application of counter-actuation methodology [8], combined with further compensation strategies [9]. These scanners operate with significantly reduced tracking range. Furthermore, the fundamentally different design of these AFMs prevents research labs with existing AFMs from accessing high speed imaging technology.

Researchers have tried to simultaneously achieve large range and high speed tracking by applying multiple actuators [10–20]. Earlier work on multi-actuation can be divided into two main categories. In one, self-actuated AFM probes are used in combination with external piezos [13,14]. This approach suffers from either the bandwidth or range limitations of bimorph actuators [13] or the complexity of attachment and actuation of magnetic nano-particles [14]. In the second category [10–12,15], two external piezo-actuators are used on independent substrates where one moves the sample and the other moves the probe. This arrangement avoids dynamic coupling, but limits the technique to only two actuators and requires modifications in the optical path of sample-scan AFMs. To control these actuators some researchers [13,15] have applied separate controllers in a nested feedback loop, with each loop controlling a single actuator. These approaches avoid the frequency bands associated with actuator dynamics and hence cannot benefit the full mechanical bandwidth of the faster actuator. Other efforts have used optimal control schemes [10,20]. Optimal control methodologies fail to accommodate the variations in AFM dynamics and imaging conditions. These variations are

* Corresponding author. Tel.: +1 617 258 6784.
E-mail address: isoltani@mit.edu (I. Soltani Bozchalooi).

http://dx.doi.org/10.1016/j.ultramic.2014.07.010
0304-3991/

caused by multiple imaging modalities, sample mass, imaging medium and ambient conditions leading to sub-optimal performance of such control techniques and increased tip–sample interaction forces.

This paper presents a simple way of incorporating additional fast actuators into an existing atomic force microscope with minimal modification. The proposed multi-actuation methodology has the following advantages: (1) there is no constraint on the number or the location of additional actuators. This flexibility opens up the applicability of multi-actuation technology to all AFM designs. (2) The control design scheme is given in a simple and general form to accommodate the flexibility described above. The method does not require installation of any additional sensors and can be implemented through simple single-input single-output (SISO) system-identification software packages. These characteristics make design and implementation of the proposed multi-actuation methodology accessible to the research labs that have functional atomic force microscopes. The control design also takes the variability in AFM dynamics into account and enables controller updating on every imaging round. (3) Upon the application of the proposed methodology a commonly used PI or PID controller is enabled to handle the dynamics of the resulting multi-actuated system. This leaves the flexibility and ease of use of this controller at user's disposal and makes the retroactive enhancement of existing AFMs an easy task.

2. Control of multiple actuators

The appealing aspect of multi-actuation for atomic force microscopy is the simultaneous achievement of large-range and high-speed tracking. In its simplest form, several actuators can be stacked in series. Fig. 1(a) demonstrates this arrangement with each actuator modeled as a second order system with an incorporated expansion force. Actuation of either of the units excites the dynamics of the other actuators. As such, compensation schemes are required to tackle these dynamics. Furthermore, the tracking responsibility needs to be divided so that the multi-component actuator mimics the behavior of a single actuator with large range and wide mechanical bandwidth. As such, the design of the multi-actuator compensation scheme aims to achieve the following criteria:

$$|P_e(\omega)| = \alpha, \quad \omega < \omega_d \tag{1}$$

where α is the low frequency gain, ω_d is the maximum frequency of interest for topography tracking and $P_e(\omega)$ denotes the frequency response of the equivalent multi-component actuator. For a z piezo-actuator that features strong dynamics over the passband, the superior performance of more complex control methodologies over conventionally used PI or PID controllers has been demonstrated [21–24]. However, one can show that when the out of plane piezo-actuator satisfies Eq. (1), a PI or PID controller meets most requirements of high speed topography tracking. Additionally, in this form, augmenting the feedback loop with feed-forward control can be very effective in improving the tracking performance [25,26]. In atomic force microscopes that lack out of plane sensing, Eq. (1) also makes sure that the z piezo-command signal can be reliably interpreted as proportional to the sample topography.

To achieve dynamics compensation for the incorporated actuators and also divide tracking responsibilities between them we propose an arrangement as illustrated in Fig. 1(b). As shown in this figure, the output of the PI control unit, u, is branched into several independent actuators, P_n, $n=1\ldots N$, with $n=1$ for the slowest and $n=N$ for the fastest actuator. The branching is done via control units, G_n, $n=1\ldots N$. In addition, these units compensate for the dynamics of the actuators and their couplings to achieve a maximally flat frequency response and hence satisfy Eq. (1). We can then write:

$$P_e = G_1P_1 + G_2P_2 + \cdots + G_NP_N = L_N \tag{2}$$

where L_N is a non-unity gain, maximally flat low-pass filter with a cutoff frequency and phase response matching those of the fastest actuator, P_N. P_e (enclosed by the dotted line in Fig. 1(b)) reflects the behavior of the equivalent multi-component actuator.

2.1. Design methodology for G_n units

The design objective is schematically shown in Fig. 2(a) where the desired output, y_d, of the equivalent actuator, P_e, is a lowpassed version of the input, u. The cutoff frequency, $\omega_c = \omega_{cN}$, and order, q_N, of the lowpass matches those of the fastest actuator, P_N. Comparing Figs. 2(a) and 1(b) one also notes the re-ordering of the actuators, P_n, and control units, G_n. This re-ordering provides a direct pathway to controller design. Now for further analysis and design, the behavior of each actuator can be reflected by its response, R_n $(n=1\ldots N)$, to a wideband input. This is shown in Fig. 2(b), where a random binary sequence represents an example of a wideband excitation. In this form, individual control units can be simply obtained through a sequence of single-input single-out system identification steps.

Assume that the frequency range over which the individual actuators are to be driven are known a priori i.e. $0\sim\omega_{c_1}$ for P_1, $\omega_{c_1}\sim\omega_{c_2}$ for P_2, etc. Upon the addition of a faster actuator, the mechanical bandwidth of the combined system extends to the maximum drive frequency assigned to that actuator e.g. upon the addition of P_2 to P_1, the mechanical bandwidth of the equivalent system changes from ω_{c_1} to ω_{c_2}, and so on. This is shown in Fig. 3, where the behavior of nth stage composed of the actuators $[P_1\ldots P_n]$ is represented by a lowpass filter, L_n with cut-off

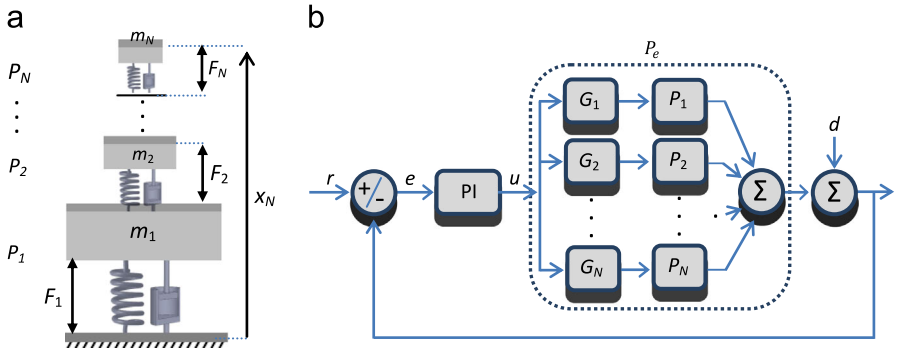

Fig. 1. (a) A simplified model of an arrangement of N actuators, $P_1\ldots P_N$, ordered from the largest/slowest to the smallest/fastest. The actuation force for P_i is represented by F_i, and (b) the control units, G_n, in series with the actuators compensate for the excited dynamics and divide the responsibilities between the actuators.

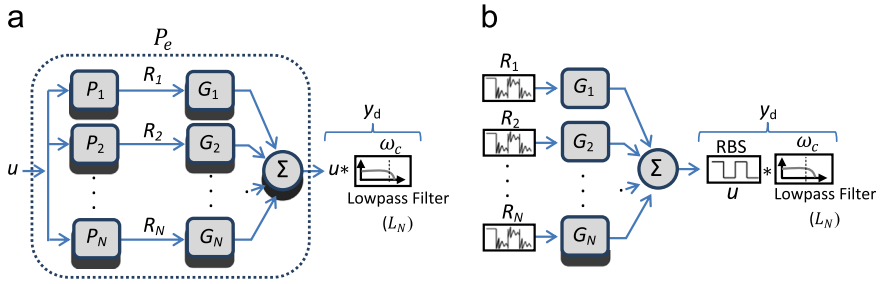

Fig. 2. (a) Desired behavior of the equivalent actuator, P_e, is reflected by the lowpass filter L_N, and (b) the behavior of each actuator, P_n, is represented by its response, R_n, to a wideband excitation such as a random binary sequence (RBS).

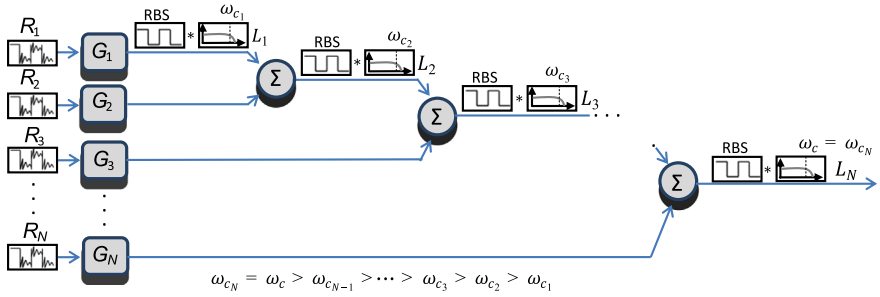

Fig. 3. With the addition of every faster actuator the cumulative bandwidth is extended up to the cut off frequency of that actuator. This fact can be utilized to significantly simplify the design process.

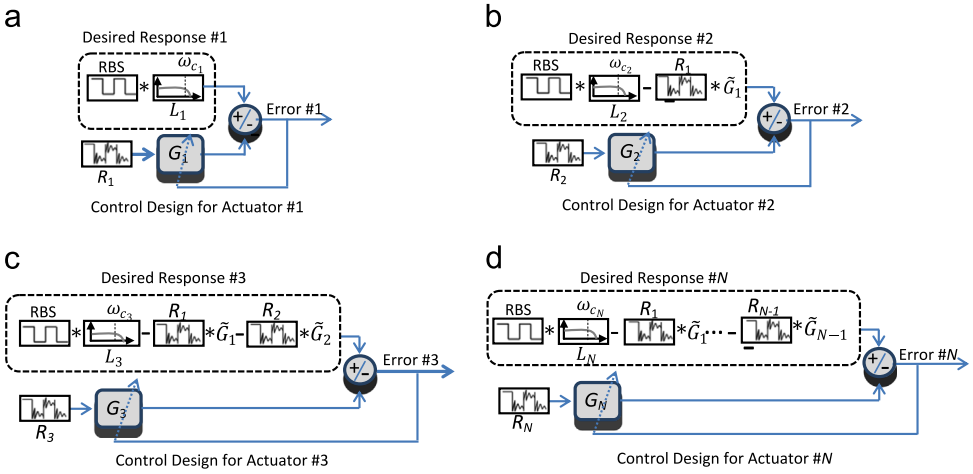

Fig. 4. Sequential design of control units (a) G_1, (b) G_2, (c) G_3, (d) G_N. ω_{c_n} represents the desired bandwidth of the nth piezo actuator.

frequency of ω_{c_n} ($\omega_{c_n} < \omega_{c_{(n+1)}}$). With this observation in mind, the individual control units G_n can be designed in a sequential manner as part of several single-input single-output (SISO) system identification problems. The design of G_1 is illustrated in Fig. 4(a) as a classic system identification problem. Following the identification of G_1, G_2 can be designed in a similar fashion as shown in Fig. 4(b). In this step the response of the first actuator should be subtracted from the desired response of the second stage. A similar approach is taken for the design of G_3 as shown in Fig. 4(c). This process is continued until all the control units, G_n, are obtained (Fig. 4(d)). The main benefit of this sequential approach is the simplified nature of the individual SISO system identification problems. The resulting problem is well studied and convex with guaranteed solution for linear systems [27]. As every frequency interval is assigned to one and only one actuator, the proposed scheme avoids the accumulation of dynamic residuals. This is important for AFM systems composed of several (more than two) actuators.

2.2. Design algorithm

The design of control units, G_n, can be summarized in the following steps:

1) Excite the individual actuators to obtain the response datasets, $\boldsymbol{R_n}$

$$\boldsymbol{R_n} = \boldsymbol{u} * \boldsymbol{h_n} \tag{3}$$

where $\boldsymbol{u}$ is a discrete set of wideband excitation signal such as a random binary sequence (RBS) with a length of M and $\boldsymbol{h_n}$ represents the impulse response associated with P_n (the nth fastest of N actuators).

2) Find the control parameters for stage n using the following equation:

$$\tilde{\boldsymbol{\theta}}_{\boldsymbol{n}} = \text{argmin}_{\theta_n} E_n(\boldsymbol{\theta_n}) \tag{4a}$$

where $\boldsymbol{\theta_n}$ is the unknown parameter vector associated with the nth controller. $E_n(\boldsymbol{\theta_n})$ quantifies the deviation of the system response from the desired response. This deviation is given as the square root of the sum of squares of the errors at individual response data-points, i.e.

$$E_n(\boldsymbol{\theta_n}) = \left(\sum_{m=1}^{M} e_n(m, \boldsymbol{\theta_n})^2 \right)^{1/2} \tag{4b}$$

Error at each point of the response dataset is given as

$$e_n(m, \boldsymbol{\theta_n}) = y_{d,n}(m) - y_n(m, \boldsymbol{\theta_n}) \tag{4c}$$

where $\boldsymbol{y}_{d,n}$ is a dataset containing samples, $y_{d,n}(m)$, $m=1\ldots M$, of the desired response of the nth actuator. The desired response of the actuator for each stage can be obtained as follows:

$$\boldsymbol{y}_{d,n} = \boldsymbol{u} * \boldsymbol{l}_n - \sum_{i=1}^{n-1} \boldsymbol{R}_i * \tilde{\boldsymbol{g}}_i \tag{4d}$$

As explained earlier, the cumulative response of the multi-actuated system at each stage is expected to be a low-passed version of the input. This is given as the first term in the above equation i.e. $u * l_n$, where $\boldsymbol{l}_n$ is a vector containing the discrete impulse response samples associated with L_n (the stage n lowpass filter). However, the actuators slower than the nth actuator are already covering the lower frequency intervals of the desired response. As such, the responses generated by these actuators should be subtracted from the desired response dataset. This is represented by the second term in Eq. (4d) i.e. $\sum_{i=1}^{n-1} \boldsymbol{R}_i * \tilde{\boldsymbol{g}}_i$, where $\tilde{\boldsymbol{g}}_i$ is a vector containing the discrete impulse response of the already designed ith controller, $G_i(\theta_i)$, $i < n$. To calculate the error data-points in Eq. (4c) one also needs the actuator response for the current estimate of the control parameters i.e. $y_n(m, \boldsymbol{\theta_n})$. A dataset containing these sample points can be obtained using the following equation:

$$\boldsymbol{y}_n(\boldsymbol{\theta_n}) = \boldsymbol{R}_i * \boldsymbol{g_i}(\boldsymbol{\theta_n}) \tag{4e}$$

The above steps should be repeated for all the remaining actuators.

A Butterworth filter is maximally flat and hence is a good choice for stage lowpass filters (to meet the requirement of Eq. (1)). For $n < N$, L_n is a 3rd order Butterworth lowpass filter with a cut-off frequency, $\omega_{c_n} = 2\omega_t$ ($\omega_{c_n} > \omega_{c_{n-1}}$) where $\angle P_n(\omega_t) < 20^\circ$ and ω_t is the transition frequency (see Appendix A). For $n=N$ (the last actuator), the order and cut-off frequency of the associated stage Butterworth, L_N, should match the roll-off of the fastest actuator. More specifically for $w = [q_N,\ \omega_{c_N}]$ where q_N is the order and ω_{c_N} the cut-off frequency of the last stage lowpass, we can write:

$$\tilde{w} = \text{argmin}_w \left\{ \sum_{m=1}^{M} (h_N(m) - l(m,w))^2 \right\}^{1/2}$$

where $h_N(m)$ and $l(m, \mathrm{w})$ are respectively samples of the impulse response vectors associated with the last actuator P_N and last stage lowpass L_N. Each design step presented by Eq. (4a) is a SISO system identification which can be implemented in either time or frequency domains with proper weighting given to various frequency bands. More details on these can be found in [9,27].

The proposed control design methodology when applied to a single actuator (Fig. 4(a)), directly leads to an inversion based compensator, without a need for an additional modeling step. As such, this same control design methodology can be utilized to tackle the lateral to out-of-plane cross-axis coupling [28] at high scan speeds.

As the proposed control design is implemented in the form of SISO system identification, all the associated limitations are naturally inherited by the method: (1) a good initial guess for the solution can significantly reduce the convergence time when solving for the optimization problem of Eq. (4a). (2) Changes in system's poles and zeros due to variations of the sample stage and sample mass necessitate control parameter update. To accelerate this step one can use the last solution as an initial guess for the current trial. (3) Proper choice of feedback loop rate is crucial. A too high of a loop rate necessitates a high order for the slower compensator, and too low values sacrifice stability and bandwidth. A rule of thumb is to select the throughput value approximately ten times the dynamics of the fastest actuator.

3. Experimental evaluation

In this section the dynamic performance and the imaging capability of a conventional AFM, operating on a tube scanner, are investigated upon the incorporation of the proposed multi-actuation scheme.

3.1. Experimental setup

The proposed multi-actuation methodology is implemented on a Bruker AS-130NM tube scanner with a lateral range of 125 μm and an out of plane range of 5 μm. A small (2 mm × 2 mm × 2 mm) piezo-stack, model PL022.30 from Physik Instrumente (PI) is used as a high speed additional actuator to improve the imaging speed of a Bruker Multi-Mode Atomic Force Microscope. The high speed actuator is enclosed in an aluminum flexure cap in order to preload the piezo-stack and protect the high voltage electrical connections when operating in fluid (Fig. 5). The flexure cap is composed of a top aluminum diaphragm (1 mm thick), and a lower pressure screw. The piezo-stack actuator is glued to the top diaphragm and then pre-loaded from the bottom by the pressure screw. Unlike earlier designs [29] the flexure cap does not include any counter-balancing piezo-actuator. This is because the excited structural dynamics are tackled through the designed compensators. Fig. 5(a), illustrates the tube scanner and the additional stack

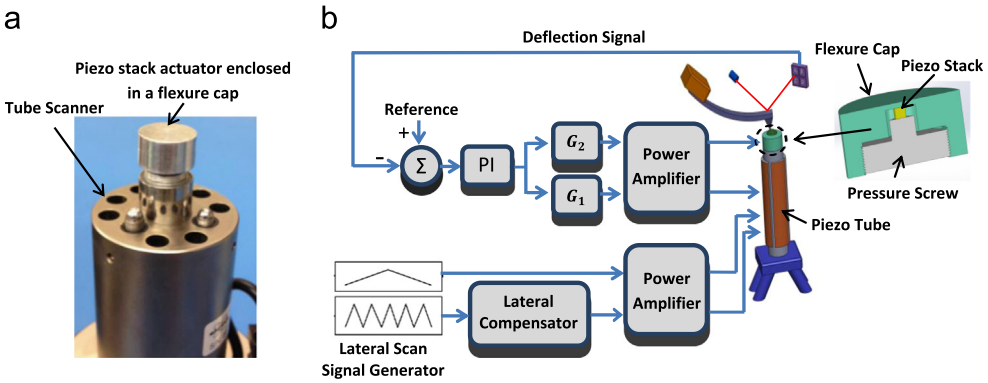

Fig. 5. (a) AS-130NM tube scanner and the additional high-speed actuator mounted on top, and (b) experimental setup.

actuator assembly mounted on top. The effective range of the piezo-stack assembly is ~1 μm. This actuator is driven by a custom made power amplifier (TechProject) with a bandwidth of 100 kHz. For the experiments the PI controller, as well as the designed units, G_1 and G_2, are implemented on a NI FlexRio FPGA platform. As shown in Fig. 5(b), a compensator, implemented on a NI PXI-7851R FPGA module, is used to tackle the cross axis coupling rooted in the lateral piezo-tube dynamics. As explained earlier, this compensator can be designed based on the proposed control design methodology implemented for a single actuator (Fig. 4(a)).

3.2. Design of G_1 and G_2

The two units, G_1 and G_2 are designed to divide the responsibilities and compensate for the excited dynamics. To measure the dynamic behavior of the individual actuators a rigid edge of the sample is brought in contact with the cantilever. As the sample and probe are in contact a wideband random binary sequence excites the tube and the stack independently. Two response datasets, R_1 and R_2 (Eq. (3)) corresponding to the tube and the stack actuators are then used according to the schematics of Fig. 4(a) and (b) and Eqs. (4a) through (4e) to design G_1 and G_2. MATLAB system identification toolbox is used for the control design. The targeted lowpass behavior of the 1st and 2nd stages (L_1 and L_2) are Butterworth filters with cut-off frequencies of $f_{c1} = 1.5$ kHz and $f_{c2} = 87$ kHz, respectively.

3.3. Dynamic performance

To assess the effectiveness of the method, we investigate the open-loop and closed loop dynamic behavior of the actuators. The black curve in Fig. 6 illustrates the open-loop dynamics of the tube, demonstrating a strong resonance at 6.2 kHz. The dynamic response of the stack actuator is superimposed on the same figure in red. As expected the stack actuator excites the dynamics of the tube (denoted by yellow dotted circles). It also demonstrates a strong resonance near 75 kHz.

The bode plot of the designed control units, G_1 (4th order) and G_2 (12th order) are illustrated in Fig. 7. The control unit, G_1, compensates for the strong tube resonance and acts as a lowpass filter. The second controller, G_2, gradually assigns actuation responsibility to the piezo-stack and compensates for the associated dynamics on the passband. The frequency response of the combined multi-actuator setup is shown in Fig. 6 (blue). A flat frequency response as expressed by Eq. (1) is achieved and the

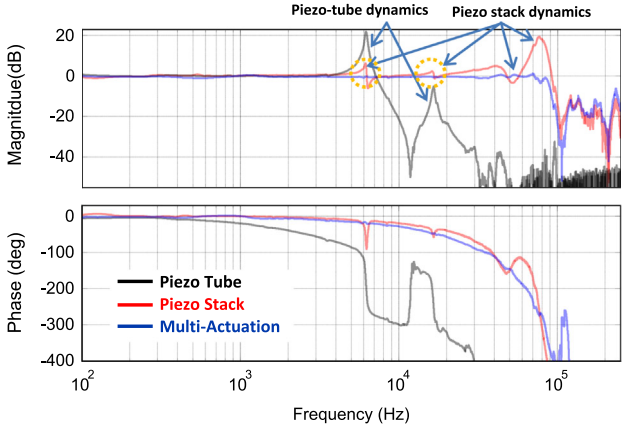

Fig. 6. Empirical transfer function plots for the piezo-tube (black), piezo-stack (red) and the combined and compensated multi-actuator setup (blue). The frequency ranges denoted by yellow circles correspond to coupling between the dynamics of the piezo-tube and the piezo-stack. (For interpretation of the references to color in this figure legend, the reader is referred to the web version of this article.)

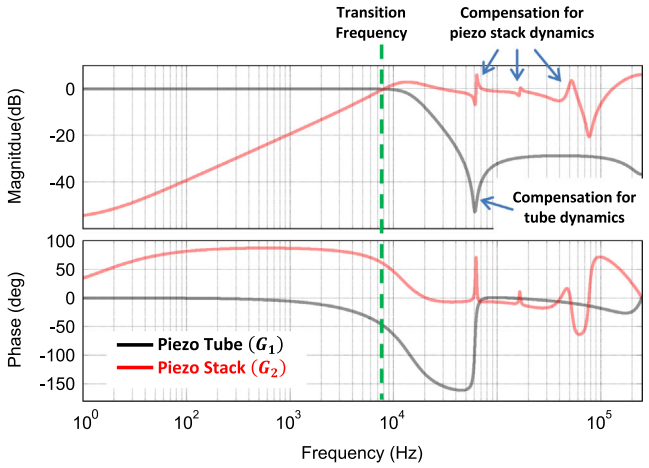

Fig. 7. Bode plots of the designed control units for the piezo-tube, G_1, (black), and piezo-stack, G_2, (red). (For interpretation of the references to color in this figure legend, the reader is referred to the web version of this article.)

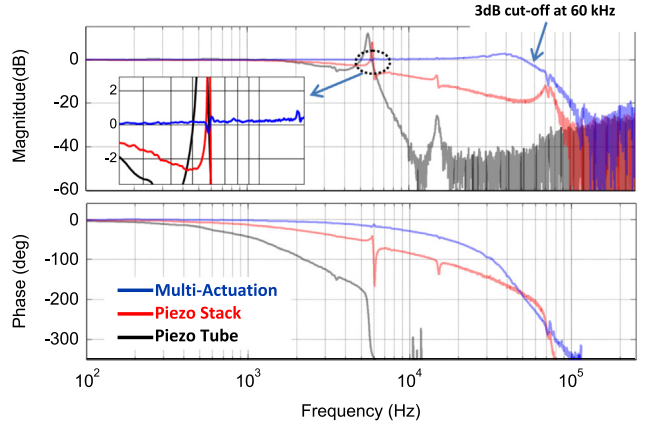

Fig. 8. Closed loop behavior of the system for the actuation of piezo-tube (black), piezo-stack (red) and multi-actuation setup (blue). (For interpretation of the references to color in this figure legend, the reader is referred to the web version of this article.)

effective bandwidth of the multi-actuator setup is extended to 87 kHz (3 dB cut-off), reflecting more than an order of magnitude improvement over that of the tube actuator alone.

To better observe the improvement in topography tracking, the closed-loop behavior of the system is evaluated when (1) the piezo-tube is used alone, (2) the piezo-stack is used alone and (3) the two actuators are combined via the designed controllers G_1 and G_2. For this purpose a probe is brought in contact with a rigid sample. Then a wideband excitation signal is injected into the loop as a variable reference set point, r (see Fig. 1(b)). The PI gains are then gradually increased until the loop shows signs of instability. Fig. 8 illustrates the closed loop behavior of the AFM system for the three cases mentioned above in black, red and blue, respectively. For case (1) the closed loop system shows strong oscillations at 5.6 kHz. This frequency is slightly higher for case (2) where strong oscillations appear at 5.9 kHz. For the multi-actuation system the closed loop bandwidth is extended to 60 kHz. A close up view of the multi-actuated closed loop frequency response near the strong dynamics of the piezo-tube demonstrates some dynamic residuals. This is rooted in the controller errors and slight nonlinearities in the system.

3.4. Imaging performance

The imaging performance of the multi-actuated setup is evaluated in contact and tapping modes, in air and in liquid. First, a

standard 3 μm-pitch square calibration grating is imaged in contact mode in air. The grating was placed on a fully flat surface to ensure that the required tracking range could be provided by the piezo-stack alone. This is to observe the influence of dynamic coupling on imaging performance. The fast scan direction is chosen perpendicular to the grating edges to introduce the highest possible disturbance bandwidth to the probe. At 3.3 mm/s tip speed the AFM probe is subject to periodic square wave disturbances with a period of $T=9e-1$ ms.

Fig. 9 shows AFM images and image section views when the isolated tube, isolated stack and the multi-actuation methodology are used. When either the piezo-tube or the stack actuator is used in isolation, the AFM is only able to react to the first few harmonics of the fundamental frequency of the disturbance input. This results in severely smoothed response of the AFM actuator, inaccurate topography estimation and large probe-sample interaction forces. This is better observed form section views of the acquired deflection images plotted in Fig. 9(d) (black and red curves). Although the mechanical bandwidth of the stack actuator can accommodate high frequency components, the dynamic coupling with the piezo-tube inhibits its closed loop operation beyond the tube resonance. This observation is also in line with the measured closed loop response of Fig. 8 (red). Given the 60 kHz closed loop bandwidth for the multi-actuation method, the AFM is able to react to the first 54 Fourier components of the disturbance. This leads to more accurate topography estimation and significantly reduced probe deflection as observed in Fig. 9(c) and the blue curve in Fig. 9(d).

Next, a sample of collagen fibrils extracted from rat tail is imaged [30]. The curved surface of this sample can introduce large tilt type height variations. The individual fibrils show 67 nm periodic banding patterns which introduce high frequency disturbances to the AFM probe when scanned at high speed. This

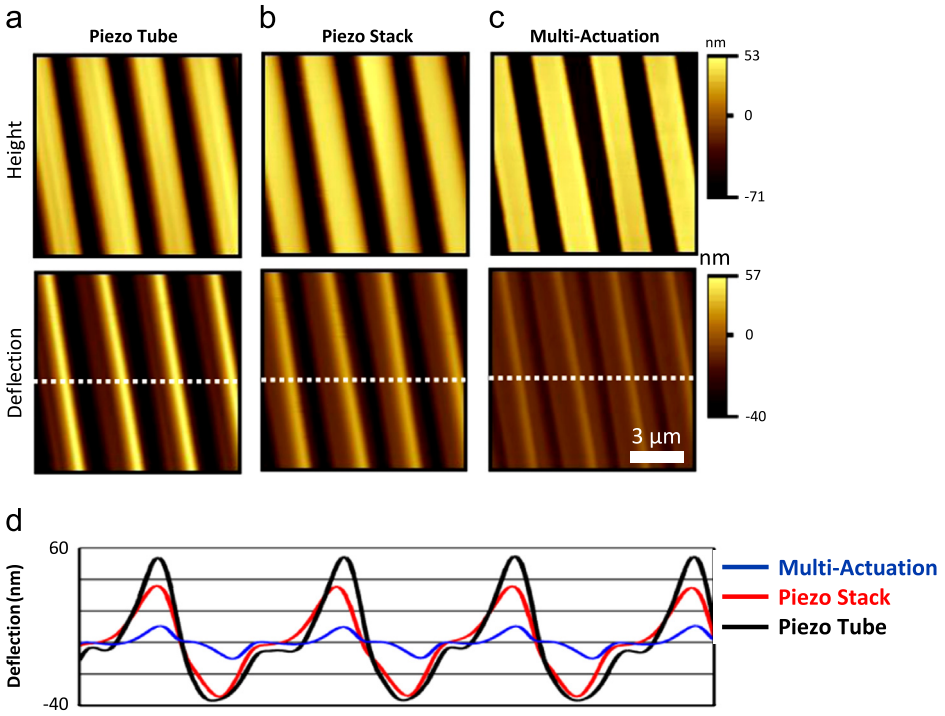

Fig. 9. AFM imaging of a 3 μm pitch calibration grating at ~3.3 mm/s tip speed (97.7 lines/s), perpendicular to the grating edges, using (a) the tube actuator, (b) the stack actuator and (c) the proposed multi-actuated setup, (d) a section (horizontal white dotted line) view of the deflection error images for the three cases presented in parts (a), (b) and (c) (images are 11 μm cutout of 16.6 μm images, taken on retrace). (For interpretation of the references to color in this figure legend, the reader is referred to the web version of this article.)

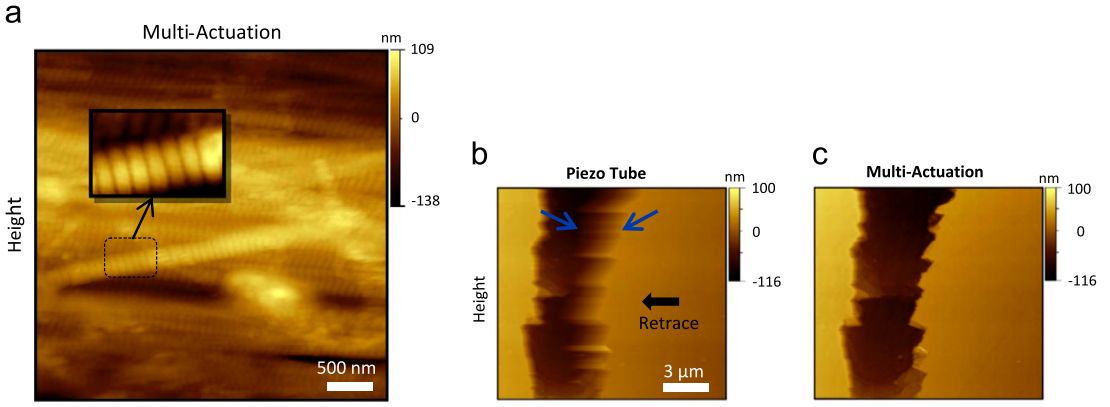

Fig. 10. (a) Retrace height image of collagen fibril extracted from rat tail, taken at 977 μm/s tip speed (97.7 lines/s), in contact mode in air using the multi-actuated setup (image is a 3.7 μm cutout of a 5 μm image), (b) retrace height image of freshly cleaved and sanded mica in tapping mode in liquid (120 kHz cantilever resonance frequency in liquid) acquired at 293 μm/s tip speed (9.77 lines/s), using conventional tube scanner alone, and (c) using the multi-actuation setup.

sample provides a good platform to test the large range and high bandwidth of the multi-actuated setup. Fig. 10(a) presents the height image (with 1st order plane fit) of collagen fibrils obtained using the multi-actuation setup at 977 μm/s tip speed. At this speed, when moving in a direction perpendicular to the 67 nm banding pattern, the tip experiences periodic disturbances with a fundamental frequency of ~15 kHz. This frequency falls well beyond the closed-loop bandwidth of the AFM when operated on the conventional tube.

The last imaging experiment is conducted in liquid, in tapping mode on a sample of freshly cleaved and sanded mica to demonstrate the effect of improved z-bandwidth in reducing the parachuting artifacts. Parachuting occurs in tapping mode when the probe loses contact with the sample on a falling edge at high imaging speed. In this period the amplitude error remains small and hence delays landing. This effect is observed in Fig. 10(b), appearing as shadows on the left side of the scratch edge. Since AFM control is open-loop during parachuting, increasing the PI gains results in faster landing without inducing instability. However, large PI gains can destabilize the loop upon landing. The image of Fig. 10(c) is taken using the multi-actuated setup. The edges of the scratch line are well defined in this image.

4. Conclusion

In this research we illustrated that high-speed, large-range imaging does not necessitate fundamental changes in the design, operation or control of conventional AFMs. To achieve high speed performance we designed a methodology to combine multiple actuators in cascaded form. This form of multi-actuation, reported here for the first time, enables the combination of a piezo-tube and piezo-stacks to form a single multi-component actuator with unified large-range and high-speed performance. This methodology implements dynamics compensation along with the division of tracking responsibilities and can significantly extend the closed loop bandwidth of AFM while maintaining a large tracking range at lower frequencies. A conventional AFM is enhanced through the proposed method by mounting a piezo-stack assembly on the tube actuator yielding an open loop bandwidth of 87 kHz and a closed loop bandwidth of 60 kHz. This bandwidth performance is on par and beyond those reported for flexure based designs but achieved on a conventional piezo-tube, benefiting from the large in-plane and out-of-plane range of these scanners. The multi-actuated setup is used to image a square calibration grating scanned perpendicular to the step edges at 3.3 mm/s tip speed, and a sample of collagen fibril scanned perpendicular to the 67 nm banding patterns at 977 μm/s. Mitigation of the parachuting phenomenon is shown on a sample of freshly cleaved and sanded mica imaged in tapping mode in liquid at 293 μm/s tip speed.

Acknowledgments

The authors would like to thank the King Fahd University of Petroleum and Minerals in Dhahran, Saudi Arabia, for funding the research reported in this paper through the Center for Clean Water and Clean Energy at MIT under Project #R16-DMN-12.

Appendix A

A.1. Stage lowpass filters: selection of cut-off frequency and order

In this appendix the selection of order and cut-off frequency for the stage lowpass filters (L_n for $n=1,\ldots,N-1$ in Figs. 3 and 4 is discussed. From earlier discussions (Fig. 4) we know that upon the successful design of G_n and G_{n+1} we can write:

$$L_n + G_{n+1}P_{n+1} \approx L_{n+1} \tag{A-1}$$

where L_{n+1} is the lowpass associated with the $(n+1)$th stage. Let us now define the transition frequency, ω_t (Fig. A1), as the frequency where the magnitudes of the first two parts of Eq. (A1) are equal, i.e. $a = |L_n(\omega_t)| = |G_{n+1}(\omega_t)P_{n+1}(\omega_t)| \le 1$. Fig. A1(a) schematically illustrates the magnitude responses of $|L_n|$, $|G_{n+1}P_{n+1}|$ and $|L_{n+1}|$ and the transition frequency, ω_t. Eq. (A-1) can be represented in vector form as shown in Fig. A1(b).

From Fig. A1(a) and (b) and assuming a gain of unity for L_n and L_{n+1} we can write:

$$a\cos\alpha + a\cos\beta = 1 \tag{A-2a}$$

$$a\sin\alpha - a\sin\beta = 0 \tag{A-2b}$$

From Eqs. (A-2a) and (A-2b) we have $\alpha=\beta$ and $a = 1/2\cos\alpha$. So $1/2 < a < 1$ and $\alpha=\beta \le \pi/3$. Fig. A2 shows a plot of gain versus phase lag at the transition frequency in red (where $a = 1/2\cos\alpha$). In the same figure the phase-magnitude response for Butterworth filters with different orders are superimposed. The intersections of the red and blue curves show the solutions to Eqs. (A-2a) and (A-2b) for various Butterworth orders. According to this figure for Butterworth orders $q_n \ge 3$ the transition frequency resides at $\alpha=\beta \approx \pi/3$ where the filter magnitude response is $a \approx 1$ (both actuators are fully active). For higher order stage lowpass filters,

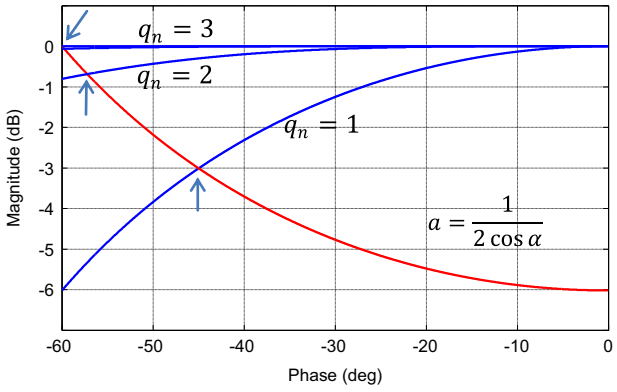

Fig. A2. Red: gain versus phase lag at the transition frequency ($a = 1/(2\cos\alpha)$), blue: phase-magnitude plot for Butterworth lowpass filters. Intersection points denote the solutions for Eqs. (A-2a) and (A-2b) for a given stage lowpass.

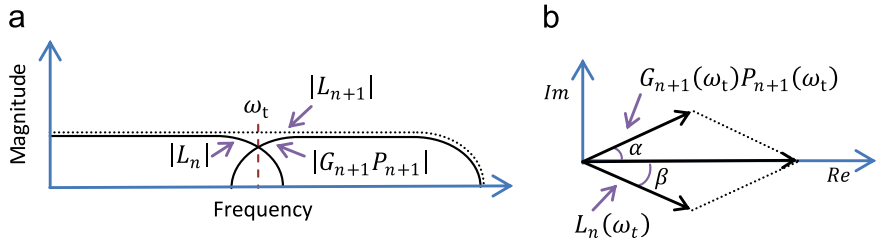

Fig. A1. Addition of the $(n+1)$th actuator and the associated frequency response summation: (a) magnitude responses and the transition frequency, ω_t, where $a = |L_n(\omega_t)| = |G_{n+1}(\omega_t)P_{n+1}(\omega_t)|$, and (b) summation in vector form, $\alpha = \angle(G_{n+1}(\omega_t)P_{n+1}(\omega_t))$, and $\beta = \angle(L_n(\omega_t))$. .

the transition frequency is shifted towards lower frequencies. Increasing the lowpass order ensures that the slow actuators deactivate at high frequencies, but results in opposing actuator efforts over a wider frequency range. To balance these effects we propose to use $q_n = 3$ for all stage Butterworth lowpass filters, L_n, $n < N$. We assume that at the transition frequency, ω_t, the slower actuator does not experience a large phase lag. As a rule of thumb one can select the transition frequency such that $\angle P_n(\omega_t) < 20^\circ$. For a 3rd order Butterworth lowpass the transition frequency (where $\alpha = \beta = \pi/3$) resides near $\omega_{c_n}/2$, where ω_{c_n} is the corresponding cut-off frequency. The cutoff frequency for the stage lowpass, L_n, can be calculated from the selected transition frequency as $\omega_{c_n} = 2\omega_t$.

References

[1] M.D. Vaudin, G. Stan, Y.B. Gerbig, R.F. Cook, High resolution surface morphology measurements using EBSD cross-correlation techniques and AFM, Ultramicroscopy 111 (8) (2011) 1206–1213.

[2] A.J. Fleming, B.J. Kenton, K.K. Leang, Bridging the gap between conventional and video-speed scanning probe microscopes, Ultramicroscopy 110 (9) (2010) 1205–1214.

[3] G. Schitter, R.W. Stark, A. Stemmer, Fast contact-mode atomic force microscopy on biological specimen by model-based control, Ultramicroscopy 100 (3–4) (2004) 253–257.

[4] M. Kobayashi, K. Sumitomo, K. Torimitsu, Real-time imaging of DNA–streptavidin complex formation in solution using a high-speed atomic force microscope, Ultramicroscopy 107 (2–3) (2007) 184–190.

[5] K.E. Aifantis, S. Shrivastava, S.H. Pelidou, Capturing the elasticity and morphology of live fibroblast cell cultures during degradation with atomic force microscopy, J. Microsc. 249 (1) (2013) 62–68.

[6] Christoph Braunsmann, E.S. Tilman, High-speed atomic force microscopy for large scan sizes using small cantilevers, Nanotechnology 21 (22) (2010) 225705.

[7] G. Schitter, K.J. Astrom, B.E. DeMartini, P.J. Thurner, K.L. Turner, P.K. Hansma, Design and modeling of a high-speed AFM-scanner, IEEE Trans. Control Syst. Technol. 15 (5) (2007) 906–915.

[8] T. Uchihashi, N. Kodera, T. Ando, Guide to video recording of structure dynamics and dynamic processes of proteins by high-speed atomic force microscopy, Nat. Protoc. 7 (6) (2012) 1193–1206.

[9] I.S. Bozchalooi, K. Youcef-Toumi, D.J. Burns, G.E. Fantner, Compensator design for improved counterbalancing in high speed atomic force microscopy, Rev. Sci. Instrum. 82 (11) (2011) 113712.

[10] G. Schitter, W.F. Rijkee, N. Phan, Dual actuation for high-bandwidth nanopositioning, in: Proceedings of the 2008 47th IEEE Conference on Decision and Control: (CDC), vols. 1–9, 2008, pp. 1782–1787.

[11] A.J. Fleming, High-speed vertical positioning for contact-mode atomic force microscopy, in: Proceedings of the 2009 IEEE/ASME International Conference on Advanced Intelligent Mechatronics, vols. 1–3, 2009, pp. 522–527.

[12] S. Kuiper, A.J. Fleming, G. Schitter, Dual actuation for high speed atomic force microscopy, in: Proceedings of the 5th IFAC Symposium on Mechatronic Systems, 2010, pp. 220.

[13] T. Sulchek, S.C. Minne, J.D. Adams, D.A. Fletcher, A. Atalar, C.F. Quate, et al., Dual integrated actuators for extended range high speed atomic force microscopy, Appl. Phys. Lett. 75 (11) (1999) 1637–1639.

[14] Y. Jeong, G.R. Jayanth, C. Menq, Control of tip-to-sample distance in atomic force microscopy: a dual-actuator tip-motion control scheme, Rev. Sci. Instrum. 78 (9) (2007) 093706.

[15] H. Mamin, H. Birk, P. Wimmer, D. Rugar, High-speed scanning-tunneling-microscopy – principles and applications, J. Appl. Phys. 75 (1) (1994) 161–168.

[16] K. El Rifai, O. El Rifai, K. Youcef-Toumi, On dual actuation in atomic force microscopes, in: Proceedings of the 2004 American Control Conference, vols. 1–6, 2004, pp. 3128–3133.

[17] A.J. Fleming, Dual-stage vertical feedback for high-speed scanning probe microscopy, IEEE Trans. Control Syst. Technol. 19 (1) (2011) 156–165.

[18] A.J. Fleming, B.J. Kenton, K.K. Leang, Ultra-fast dual-stage vertical positioning for high performance SPMs, in: Proceedings of the 2010 American Control Conference, 2010, pp. 4975–4980.

[19] Y. Yan, Y. Wu, Q. Zou, C. Su, An integrated approach to piezoactuator positioning in high-speed atomic force microscope imaging, Rev. Sci. Instrum. 79 (7) (2008) 073704.

[20] S. Kuiper, G. Schitter, Model-based feedback controller design for dual actuated atomic force microscopy, Mechatronics 22 (3) (2012) 327–337.

[21] D.Y. Abramovitch, S.B. Andersson, L.Y. Pao, G. Schitter, A tutorial on the mechanisms, dynamics, and control of atomic force microscopes, in: Proceedings of the 2007 American Control Conference, vols. 1–13, 2007, pp. 965–979.

[22] S.M. Salapaka, M.V. Salapaka, Scanning probe microscopy, IEEE Control Syst. 28 (2) (2008) 65–83.

[23] S. Devasia, E. Eleftheriou, A. Moheimani SOR, Survey of control issues in nanopositioning, IEEE Trans. Control Syst. Technol. 15 (5) (2007) 802–823.

[24] G.M. Clayton, S. Tien, K.K. Leang, Q. Zou, S. Devasia, A review of feedforward control approaches in nanopositioning for high-speed SPM, J. Dyn. Syst. Meas. Control 131 (6) (2009) 061101.

[25] G. Schitter, A. Stemmer, F. Allgower, Robust 2 DOF-control of a piezoelectric tube scanner for high speed atomic force microscopy, in: Proceedings of the American Control Conference, 2003.

[26] Y. WuQingze Zou, Robust inversion-based 2-DOF control design for output tracking: piezoelectric-actuator example, IEEE Trans. Control Syst. Technol. 17 (5) (2009) 1069–1082.

[27] L. Ljung, System Identification: Theory for the User, 2nd edition, Prentice Hall, UpperSaddle River, NJ, 1999.

[28] Y. Wu, J. Shi, C. Su, Q. Zou, A control approach to cross-coupling compensation of piezotube scanners in tapping-mode atomic force microscope imaging, Rev. Sci. Instrum. 80 (2009) 4.

[29] B.J. Kenton, A.J. Fleming, K.K. Leang, Compact ultra-fast vertical nanopositioner for improving scanning probe microscope scan speed, Rev. Sci. Instrum. 82 (2011) 12.

[30] I. Revenko, F. Sommer, D.T. Minh, R. Garrone, J. Franc, Atomic force microscopy study of the collagen fibre structure, Biol. Cell 80 (1) (1994) 67–69.